Mon. Not. R. Astron. Soc. **000**, 1–16 (2013) Printed 16 May 2014 (MN LATEX style file v2.2)

The Herschel view of circumstellar discs: a multi-wavelength study of Chamaeleon I

Donna Rodgers-Lee[1⋆], Alexander Scholz[1,2], Antonella Natta[1,3], Tom Ray[1]
[1] *School of Cosmic Physics, Dublin Institute for Advanced Studies, 31 Fitzwilliam Place, Dublin 2, Ireland*
[2] *School of Physics and Astronomy, University of St. Andrews, North Haugh, St Andrews, Fife KY16 9SS*
[3] *INAF - Osservatorio Astrofisico di Arcetri, Largo E. Fermi 5, I-50125 Firenze, Italy*

arXiv:1405.3833v1 [astro-ph.SR] 15 May 2014

Accepted 2014 May 6. Received 2014 April 21; in original form 2014 January 15

ABSTRACT

We present the results of a multi-wavelength study of circumstellar discs around 44 young stellar objects in the 3 Myr old nearby Chamaeleon-I star-forming region. In particular, we explore the far-infrared/submm regime using Herschel fluxes. We show that Herschel fluxes at 160-500 μm can be used to derive robust estimates of the disc mass. The median disc mass is 0.005 $M_\odot$ for a sample of 28 Class IIs and 0.006 $M_\odot$ for 6 transition disks (TDs). The fraction of objects in Chamaeleon-I with at least the 'minimum mass solar nebula' is 2-7%. This is consistent with previously published results for Taurus, IC348, ρ Oph. Diagrams of spectral slopes show the effect of specific evolutionary processes in circumstellar discs. Class II objects show a wide scatter that can be explained by dust settling. We identify a continuous trend from Class II to TDs. Including Herschel fluxes in this type of analysis highlights the diversity of TDs. We find that TDs are not significantly different to Class II discs in terms of far-infrared luminosity, disc mass or degree of dust settling. This indicates that inner dust clearing occurs independently from other evolutionary processes in the discs.

Key words: circumstellar matter – stars: formation – stars: pre-main-sequence – infrared: stars – techniques: photometric.

1 INTRODUCTION

Young stellar objects (YSOs) are an area of intense research as it is in the early stages of star formation that planetary systems are formed. The evolution of YSOs is often described using three main stages (Lada 1987; Adams et al. 1987): Class I sources are thought to represent the earliest stage where the protostar is deeply embedded in an envelope of dust and gas which strongly accretes onto a circumstellar disc. Class II objects possess a circumstellar disc with lower accretion rates and the envelope has mostly disappeared. Class III objects no longer possess a circumstellar disc, or the disc is at least vastly dissipated. There have been further stages added such as Class 0 which is thought to be an earlier evolutionary phase than that of Class I (André et al. 1993). Another classification is that of flat spectrum sources which are thought to represent an evolutionary stage between Class I and Class II.

The circumstellar discs around Class II objects evolve primarily due to viscosity, but also because of a number of other physical processes such as grain growth, dust settling, dissipation by photoevaporation and the formation of planets may take place. The evidence and effect of these physical processes are observable in the spectral energy distribution (SED) of YSOs (Watson et al. 2007; Dominik et al. 2007; Williams & Cieza 2011).

In this context, the frequently discussed transition discs (TDs, see Section 7 in Williams & Cieza (2011) and references therein) play an important role. TDs were first identified from their SEDs which show a large deficit of emission in the near- and mid-infrared when compared to the median SED of Class IIs in the same star forming region. In some cases, millimetre interferometry data shows an inner cavity (e.g. Brown et al. 2007). TDs are often considered to be a later evolutionary stage than Class II as the circumstellar disc is thought to have been cleared out by the formation of a planet (Rice et al. 2003; Quillen et al. 2004), but there are many other viable possibilities. Stellar-mass companions (Mathieu et al. 1997; Ireland & Kraus 2008), dust coagulation and evolution (Dullemond & Dominik 2005; Krauss et al. 2007), inside-out evacuation by the magnetorotational instability (Chiang & Murray-Clay 2007) or photoevaporation (Alexander et al. 2006; Alexander & Armitage 2007) could also be responsible. The possibility of observ-

⋆ E-mail: donna@cp.dias.ie

ing and understanding the early stages of planet formation makes TDs some of the most interesting YSOs to study.

The availability of fluxes from the PACS and SPIRE instruments of the Herschel Space Observatory (Pilbratt et al. 2010; Poglitsch et al. 2010; Griffin et al. 2010) gives us the opportunity to study for the first time the full SED for large numbers of YSOs. For Class II objects, the stellar photosphere is prominent from optical to near-infrared (NIR) wavelengths whereas the emission from circumstellar discs dominates in the mid-infrared (MIR) and far-infrared (FIR). The combination of 2MASS, DENIS, Spitzer, WISE, Herschel, LABOCA and mm data allows us to examine the entire emission spectrum of the discs. Depending on the wavelength range, different physical parameters can be investigated. In particular, the Herschel wavelength domain allows us to investigate the geometry of the outer discs and their disc masses. The inclusion of Herschel data also allows us to re-examine the classification of YSOs.

In this paper we aim to investigate circumstellar discs using a multi-wavelength dataset, including Herschel fluxes, for objects in the star forming region Chamaeleon-I. The purpose of this study is to examine the discs using the full SED, to provide criteria to facilitate the study of larger samples, and to characterise possible targets for detailed follow-up observations, e.g., with the new submm/mm interferometer ALMA. We describe our sample of YSOs in Section 2. The construction and appearance of the SEDs is discussed in Section 3. Section 4 illustrates spectral slope diagrams making use of the Herschel data. Section 5 investigates the fractional disc luminosities at Herschel wavelengths. We discuss the possibility of Herschel data tracing the mass of the disc and we present our results for the disc masses in Section 6. Section 7 focuses on fitting the SEDs of the TDs in our sample. Complementary information is given in the appendices.

2 DESCRIPTION OF SAMPLE

The Chamaeleon-I (Cha-I) star-forming region contains a well studied sample of YSOs, with a median age of ~ 3 Myr (Luhman 2007), at a distance of ~ 160 pc (Whittet et al. 1997). It suffers little extinction which makes it an ideal region to study YSOs. Winston et al. (2012) present Herschel data for 49 YSOs in Cha-I. The data are from the Herschel Gould Belt survey (André et al. 2010) which has covered the entire Cha-I cloud. We will not consider in the following a B9.5 star (T32) and the object T54 which suffers from extended source contamination (Matrà et al. 2012). We exclude ESO Hα 569 which we confirm to be an edge-on disc (see Appendix B1). In addition, we exclude ISO 237 and Hn10e which suffer from contamination (see Appendix B1). For a full list of the 44 objects in our sample and their derived properties see Table A1.

The temperatures, luminosities and extinctions (A_J) were obtained for 35 out of our 44 objects from Luhman (2007). The stellar properties are used in Section 5, i.e. only 35 objects are considered in this section. The size of the sample being considered in each section will be listed at the beginning of the section for clarity.

The temperature range of our sample is from $\sim 3090 - 5860$ K and the spectral types range between G2 − M5.25, as shown in Fig. 1. This means the sample covers a mass range of $\sim 0.1 - 2.0$ $M_\odot$. From the list in Winston et al. (2012) we also take the SED classification for these objects. They comprise 29 Class IIs, 6 flat spectrum (FS) sources, 2 Class II/TD, 1 TD, 4 Class Is, 1 Class 0 and 1 Class III. The original source of these classifications is Luhman et al. (2008). Note that these classes are based on Spitzer data only (i.e. up to $\lambda = 24\,\mu$m).

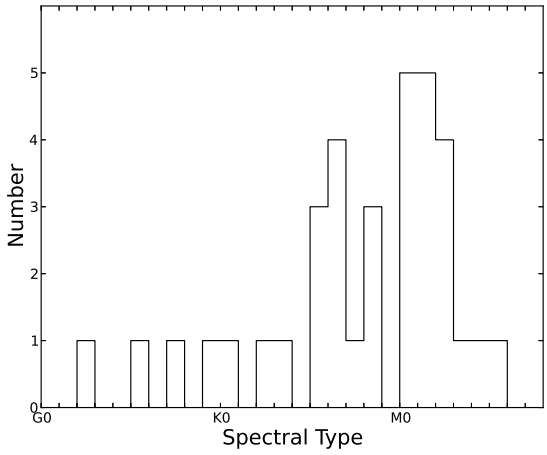

Figure 1. Distribution of different spectral types (Luhman 2007) for our sample.

Recently Ribas et al. (2013) published Herschel data for 9 objects, 8 of which are in our sample. Their fluxes are somewhat different (on average 18% higher at 70 μm) than in Winston et al. (2012), possibly due to different data reduction techniques. We also note that 12 of the sources analysed here are also contained in the 17-object sample discussed in a recent paper by Olofsson et al. (2013). They focus on the low mass stars and brown dwarfs in Cha-I, consequently all 12 are M dwarfs and at the low-mass end of the spectrum covered in our paper. Olofsson et al. (2013) analyse the disc SEDs with Herschel/PACS data using radiative transfer modeling, and some of their results are complementary to ours.

Our list of objects is not a complete sample of all YSOs in Cha-I. First, we are only analysing objects detected by Herschel. From Winston et al. (2012) the Herschel detection limit was adopted to be $\sim$0.1 Jy at all bands which corresponds to a spectral energy density detection limit of 4.3×10^{-12}erg sec^{-1} cm^{-2} at 70 μm. Objects with discs fainter than this detection limit are missing if they exist. Second, as discussed above, 9 objects do not have stellar properties listed in Luhman (2007) and are excluded from the analysis in Section 5. The luminosity bias in the far-infrared also results in missing most of the very low mass members of Cha-I. This is obvious from the Hertzsprung-Russell (HR) diagram of all the known objects in Cha-I (Luhman 2007), as shown in Fig. 2. In this diagram, the objects in our sample are marked in red. The two outliers from our sample in the HR diagram are ESO Hα 569 and HH48. These 2 objects are discussed further in Appendix B1, along with their SEDs.

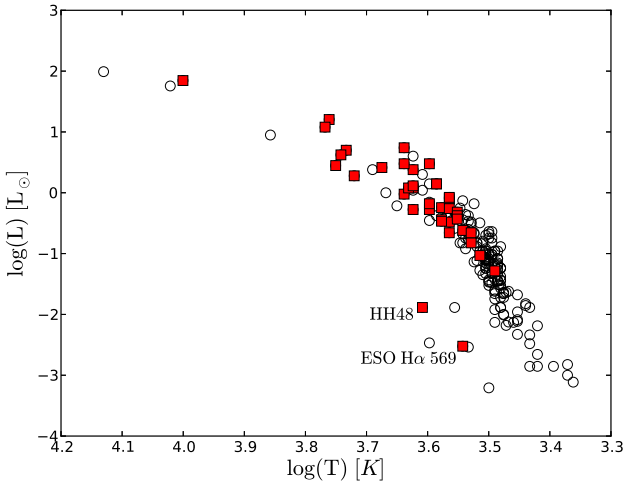

Figure 2. HR diagram of Cha-I: Open circles represent all known YSOs in Cha-I, from Luhman (2007), red squares are the objects in our sample. The two underluminous outliers are labelled. ESO Hα 569 is one of the objects excluded from our sample.

3 SPECTRAL ENERGY DISTRIBUTIONS

We constructed SEDs for the sample using DENIS, 2MASS, WISE, Spitzer, Herschel, LABOCA and 1300 μm data where available, see Table 1 for a complete list of the photometry used. 23 out of the 44 objects have 870 μm or 1.3 mm data. We also used Spitzer IRS (Houck et al. 2004) data where available. The extinction law from Cardelli et al. (1989) with $R_V = 3.1$ was used to deredden the data points.

Some of the objects in our sample were observed by Belloche et al. (2011) using LABOCA, which has an angular resolution of 19.2$''$. We took any matches with 2MASS coordinates within $\sim 5''$. Seventeen objects were matched, but with this criterion, 2 objects are clearly misassociated (ESO Hα 559 and 2MASS J11064658-7722325). This was decided by looking at the full SEDs for these objects and the LABOCA flux density for these objects was not used.

3.1 Modeling the photospheric SED

The first aim was to correctly determine the stellar photosphere component from the entire SED. This made it possible for us to examine the dust component of the SED to compute disc luminosities and compare it with models. The stellar component of the SED was constructed using BT-NextGen[1] model atmospheres from Allard et al. (2012) with log g = 3.5, for all objects. The flux densities given by the model atmospheres were multiplied by a dilution factor of $(R_{star}/D)^2$, where R_{star} is the radius of the star and D is the distance to the star (160 pc). The radius of the star was calculated using the temperature and luminosity given in Luhman (2007). There were no further adjustments made to fit the SEDs (e.g., no normalisation). The NIR data were used to check that the model atmosphere chosen for the object fit the data. For 30 out of the 35 objects, the photospheric model fit the datapoints reasonably well, which confirms the validity of the assumed stellar properties. The remaining 7 show significant deviations, most likely due to variability. The optical and NIR photometry in the literature for Cha-I originates from observations spanning more than two decades. On these timescales, most YSOs show variations up to 30%, and a subsample even more (Scholz 2012). For the 7 objects in question we obtained a new set of photometry, which is discussed in Appendix C. All seven are confirmed as variable stars, two of them with large amplitudes of > 1 mag.

[1] http://phoenix.ens-lyon.fr/simulator/index.faces

3.2 SEDs for typical YSOs

The SEDs in our sample show great diversity. In Fig. 3 we show 3 examples from our sample illustrating a typical Class I, Class II and TD. Objects similar to Fig. 3 (a) with a rising SED through the NIR and MIR are identified in the literature as Class 0 or Class I. This strong excess cannot be explained by a disc alone and is at least partly caused by a circumstellar envelope. The majority of the sample resembles Fig. 3 (b) with excess at all IR wavelengths, but declining SEDs. These are typical Class IIs, the IR emission is consistent with being produced by a circumstellar disc.

A third type of SED is shown in Fig. 3 (c). This object, T21, shows negligible excess emission above the photospheric level in the NIR to MIR. It has steeply increasing flux densities around 10-20 μm, and beyond 70 μm an SED similar to Class IIs. This is the typical appearance of TDs. It is usually explained by an opacity hole in the inner disc (see Section 1). This object is categorized as Class III by Luhman et al. (2008) based on the photometry in the mid-infrared, but was already noted as TD by Kim et al. (2009) using the IRS spectrum (5-38 μm).

These three objects represent three different stages in disc evolution. However, there are other objects which are not as easily classified. In Section 4, using Herschel data, we demonstrate that there is a continuum of objects between these clearly distinct examples of Class I, Class II and TD.

4 SPECTRAL SLOPES AND DISC EVOLUTION

Spectral slopes were examined, making use of the Herschel data, to classify and characterise the objects in our sample. In the following discussion the spectral slope is defined as (Adams et al. 1987):

$$\alpha_{\lambda_1-\lambda_2} = \frac{\log(\lambda_1 F_{\lambda_1}) - \log(\lambda_2 F_{\lambda_2})}{\log(\lambda_1) - \log(\lambda_2)} \quad (1)$$

We have plotted α_{12-70} against α_{K-12} in Fig. 4 and α_{K-12} against α_{K-70} in Fig. 5 as possible ways to (a) separate the various different classes of objects and (b) to illustrate the effects of the physical processes that affect the discs. The classifications used in the figures come from Luhman et al. (2008) for the Class Is and flat spectrum sources. We have not labelled the known TDs and Class IIs differently. Both diagrams show a clear 'Class II locus' around (-1,-1), where the bulk of our sample is located.

Table 1. List of photometry sources and relevant wavelengths

Telescope/Survey	Instrument	$\lambda[\mu m]$/band	Ref.	Zero-point flux [Jy]	Ref.
-	-	R, V	1	2870.0, 3540.0	11
HST	-	0.56	2	-	-
DENIS	-	I, J, K	3	2499.0, 1595.0, 665.0	3
2MASS	-	J, H, K	4	1594.0, 1024.0, 666.7	12
WISE	-	3.4, 4.6, 12.0, 22.0	5	309.540, 171.787, 31.674, 8.363	13
Spitzer	*IRAC*	3.6, 4.5, 5.8, 8.0	6	280.9, 179.7, 115.0, 64.13	14
	MIPS	24	6	7.17	14
Herschel	*PACS*	70, 160	7	-	-
	SPIRE	250, 350, 500	7	-	-
APEX	LABOCA	870	8,9	-	-
-	-	1300	10	-	-

[1] Gauvin & Strom (1992), [2] Robberto et al. (2012), [3] Fouqué et al. (2000), [4] Skrutskie et al. (2006), [5]Wright et al. (2010) , [6] Luhman et al. (2008), [7] Winston et al. (2012), [8] Belloche et al. (2011), [9] Cieza et al. (2013), [10] Henning et al. (1993), [11] Skinner (1996), [12] Cohen et al. (2003),[13]Jarrett et al. (2011),[14] http://irsa.ipac.caltech.edu/Missions/spitzer.html

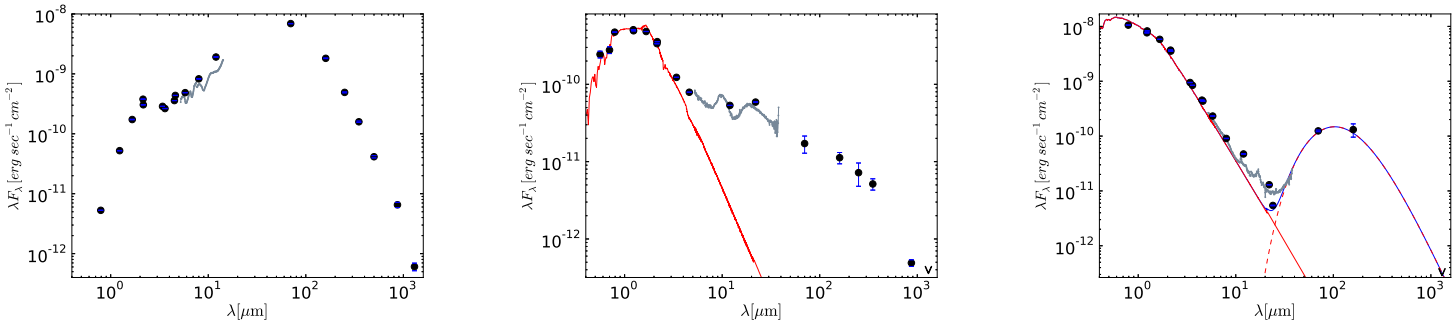

(a) IRN/P24, Class I (b) SY Cha, Class II (c) T21, TD

Figure 3. Variety of SEDs for our sample. The red lines are the model atmospheres from Allard et al. (2012). For T21 the dotted red line is the simple model fit (see Appendix C1) and the blue line is combination of both.

In both diagrams three broad trends are visible. First, there seems to be a continuous trend from the upper right (where the Class I objects appear) to the Class II locus. This slope reflects the drop in the high levels of NIR/MIR emission observed in the SED and the evolution from rising SEDs in the Class Is to declining SEDs in the Class IIs. This change cannot be explained with an evolution of the discs themselves. The most likely explanation is the gradual disappearance of the circumstellar envelope. The arrow labelled 'envelope depletion' is merely indicative of the effect we believe that envelope depletion would have and does not correspond to any model data points. The approximate line between Class I and flat spectrum/Class IIs is at $\alpha_{K-12}, \alpha_{K-70} \approx 0$, but the diagrams do not show a clear separation between Class I and Class II.

Second, in both spectral slope plots, the Class IIs show a broad scatter of about 1 order of magnitude on both axes. The scatter is most likely caused by the evolution from flared to flat discs, possibly caused by dust settling (Dullemond & Dominik 2004; D'Alessio et al. 2006). We investigated the changes in the SEDs due to settling using 2-layer disc models (Chiang & Goldreich 1997, 1999; Dullemond et al. 2001) with different dust populations in the surface and midplane of the disks, as described in Ricci et al. (2010), where the details of the adopted dust model can also be found. The small grains on the disk surface have a dust-to-gas ratio of 0.01 in fully flared models. We describe the settling by decreasing this ratio by a constant factor ϵ, as in D'Alessio et al. (2006), from 1 (fully flared models which is the upper dash on the arrows in Figs. 4, 5) to 0.1, 0.01, 0.001 (the lower dash on the arrows in Figs. 4, 5) respectively. Using this model we found that a fully flared disc around a Class II source with characteristics typical for our sample (SY Cha in Fig. 3) sits at the upper right corner of the Class II 'clump' in both diagrams. On the other hand, a Class II with an almost flat disc sits at the lower left corner of the Class II 'clump'. This indicates that all the scatter in α_{12-70} and α_{K-70} and a large part of the scatter in α_{K-12} can be explained by varying the degree of flaring. Conversely, if settling is indeed the physical underlying process the scatter can be explained by varying its efficiency. An arrow in both diagrams, which corresponds to the position and spans the range of model data points, indicates the direction of increasing dust settling. Olofsson et al. (2013) find a distribution in the amount of flaring in their sample of M dwarfs from Cha-I, similar to our result.

Seven objects in these diagrams are labelled (SZ Cha, CS Cha, T21, T25, T35, ESO Hα 559 and ISO 52). These labelled objects are located above (in Fig. 4) and to the left (in Fig. 5) of the Class II locus. For this group α_{12-70} is higher than for the Class II group, but α_{K-12} is lower, i.e. there is evidence for a flux deficit in the NIR/MIR. There-

fore, all these objects should be considered to be TDs. While the most extreme outliers in this group are well-known TDs (e.g. T21, see Section 3.2), others occupy the colour space between these prototypical TDs and Class II. For a more detailed discussion and the SEDs of these labelled objects, see Section 7 and Fig. 11.

Ribas et al. (2013) use an analogue of Fig. 4 to introduce a sharp distinction between TDs and Class II discs. In our figure, this separation is seen at:

$$\begin{aligned} \alpha_{12-70} &\gtrsim 0 \text{ for TD objects} \\ \alpha_{12-70} &\lesssim 0 \text{ for Class II objects} \end{aligned} \quad (2)$$

However, we note that there is no obvious gap in the diagram between Class IIs and TDs, thus, the spectral slope threshold given above is arbitrary and can only be used to classify the most extreme objects. Both diagrams show a continuum of datapoints from the Class II locus to the typical TDs. Objects like SZ Cha and ISO 52 (for their SEDs see Fig. 11) are located in this transition area. This smooth transition from Class II to TD is also visible in Fig. 5.

Using the simple disc model of Beckwith et al. (1990) which is described in Appendix C1, we aim to explain the difference between Class IIs and TDs in the spectral slope diagrams by assuming that the TDs are affected by inner disc clearing. We adopt plausible parameters for the central source and the global properties of the discs. These plausible parameters are the fiducial values mentioned in Appendix C1. We only vary the inner radius of the discs, from about 0.4 AU to 1.5 AU. In Figs. 4 and 5 an arrow illustrates the effect of an increasing inner disc radius on the spectral slope values. The arrow spans the range of the inner radii used in the model. Clearly, the presence of inner holes of varying sizes alone can broadly explain the phenomenological difference between Class IIs and TDs. For a more detailed discussion of the inner hole sizes and the nature of these gaps, we refer the reader to Section 7.

The spread in the TDs α_{K-70} spectral slope is similar to that of the Class IIs. This slope is mostly unaffected by the inner disc clearing. The spread can again be explained by varying degree of dust settling, as for the Class IIs (see above). Thus, dust settling affects Class IIs and TDs in a similar way. Based on this finding, it seems plausible that the clearing of the inner disc, which may be due to a variety of processes, occurs independently from the settling process in the discs. This is in line with one of the conclusions in the study by Sicilia-Aguilar et al. (2013), based on NIR and MIR data.

We also examined spectral slope diagrams using the data at $\lambda \geqslant 70\,\mu$m, but found no noticeable difference between TDs and the rest of the sample. As an example, we plotted α_{70-250} against α_{K-12} in Fig. 6. At these long wavelengths, the spectral slopes of Class Is, Class IIs, and TDs are well mixed. Thus, the bulk of the dust in the outer disc, which determines the flux densities and spectral slopes at the submm/mm wavelengths, remains unaffected by whatever process causes the clearing in the inner part of the disc.

Note that Class IIIs and sources with only photospheric emission or very little infrared excess (e.g. from debris discs) would appear in the lower left corner of the diagrams which are not populated by our sample due to the lack of sensitivity in the Herschel survey.

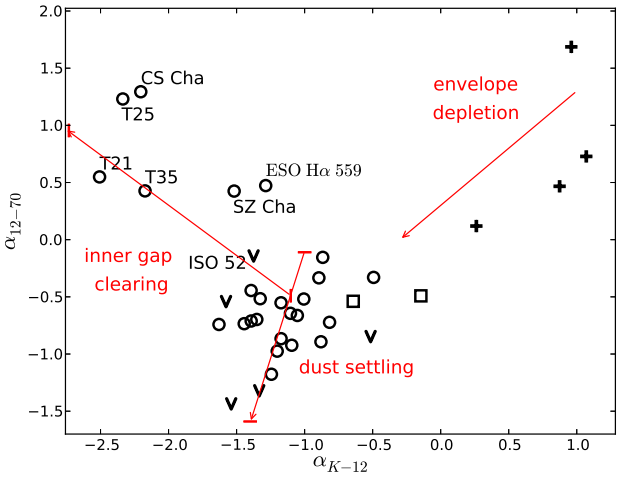

Figure 4. Spectral slope diagram of entire sample: '+' are Class Is, '□' are flat spectrum sources, '○' are Class IIs and TDs,'∨' are upper limits. Objects that will be discussed in Section 7 are labelled.

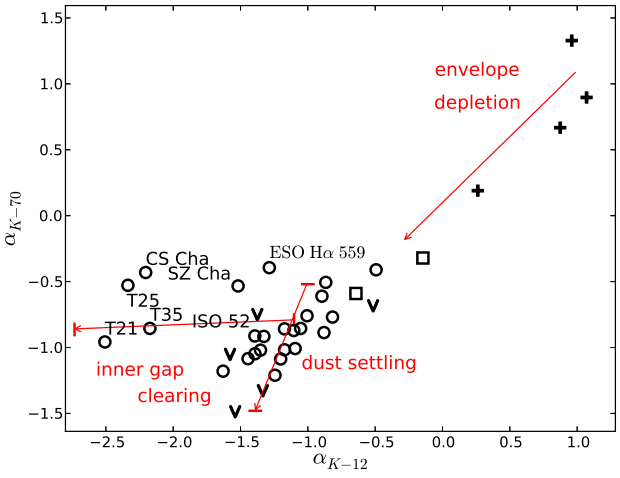

Figure 5. Spectral slope diagram of entire sample: with symbols as in Fig. 4

5 DISC LUMINOSITIES

The luminosity of each disc was calculated to examine possible trends of luminosity with object class. Nine objects were omitted (which includes all 4 Class I objects) for the reasons discussed in Section 2, i.e. a sample of 35 objects remains.

The stellar luminosities were computed using the flux densities from the model atmospheres so that the stellar luminosity can be subtracted from the total luminosity of each object. $L_{star}(\lambda_1, \lambda_2)$ is the stellar luminosity, between $\lambda_1 = 0.1\,\mu$m and $\lambda_2 = 1000\,\mu$m, which was calculated by integrating over the model atmosphere flux density values and multiplying by $4\pi D^2$, where D is the distance to the star. The interpolation between data points is a straight line. Our luminosities were compared with the values from Luhman (2007); 95% were within 10% of these luminosities

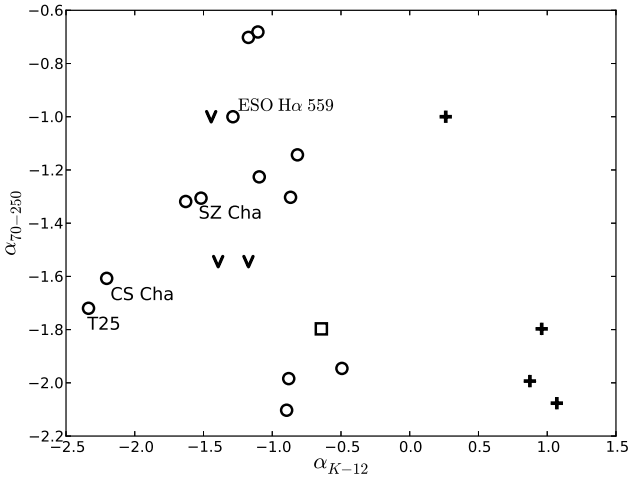

Figure 6. Spectral slope diagram of entire sample: with symbols as in Fig. 4

and 64% were within 5%. Given the different method used to compute the stellar luminosities our values are acceptable.

The disc luminosity, $L_{disc}(\lambda_1, \lambda_2)$, between two particular wavelengths, λ_1, λ_2, was then calculated as follows:

$$L_{disc}(\lambda_1, \lambda_2) = L_{both}(\lambda_1, \lambda_2) - L_{star}(\lambda_1, \lambda_2) \qquad (3)$$

where $L_{both}(\lambda_1, \lambda_2)$ is the total luminosity (the stellar and disc contributions combined) between λ_1, λ_2, calculated by integrating between the flux density data points for these wavelength values. In the FIR regime the stellar luminosity is small in comparison to the luminosity of the disc so $L_{disc}(\lambda_1, \lambda_2)$ will be most accurate there. In the NIR $L_{disc}(\lambda_1, \lambda_2)$ is very sensitive to the exact value of the photospheric contribution; it is difficult to quantify any disc contribution to the overall luminosity at these shorter wavelengths. We therefore do not examine disc luminosities for $\lambda < 8\,\mu$m. The fractional disc luminosity is defined as $L_{disc}(\lambda_1, \lambda_2)/L_{star}$, where L_{star} is the total stellar luminosity.

We plotted various combinations such as $L_{disc}(8, 12)/L_{star}$ and $L_{disc}(160, 250)/L_{star}$, as shown in Figs. 7 (a), (b). In these plots, the same objects as in Section 4 are labelled. As pointed out in Section 4, all these objects can be considered to be TDs with evidence of inner disc clearing.

These figures show no correlation between fractional disc luminosity and total stellar luminosity. Fig. 7 (a) indicates that most TDs are underluminous between $8 - 12\,\mu$m which is to be expected. However, in Fig. 7 (b) most of them are indistinguishable from other Class IIs. This implies that in the FIR the energy output of TDs is the same as Class IIs, confirming that inner disc clearing is independent from the evolution of the outer disc.

One of the objects that we have classed as a TDs, ESO Hα 559, is overluminous in comparison to the rest of the TDs at the Herschel wavelength regime (see Fig. 7, both panels). There is no evidence that this object is seen edge-on, i.e. inclination effects are not a plausible explanation for this anomaly. One option is that this a strongly flared disc with only a small inner hole.

In contrast to what Fig. 7 (b) shows (that the TDs are well mixed) Ribas et al. (2013) found that the TD flux densities at 70 and 160 μm were larger than the median flux density of Class IIs. A combination of the following three effects could potentially resolve this discrepancy: (1) Ribas et al. (2013) are examining a sample of objects from Cha-I and Cha-II whereas our sample is only sources from Cha-I. (2) As mentioned in Section 2 the flux densities reported in Ribas et al. (2013) are systematically higher than the flux densities in Winston et al. (2012) for the TDs, which we are using. Ribas et al. (2013) do not list the flux densities for the Class IIs, i.e. we cannot decide on this particular issue. (3) We are also examining the luminosity between 160-250μm and not between 70-160μm. We also note that the samples are quite small, i.e. it is difficult to establish significant differences.

The disc luminosity is $\sim 0.1 - 0.2\,L_{star}$ for our sample between 8 and 500 μm. In comparison, debris discs, which are the discs formed from remnant discs by planetesimal collisions, have been found to be $\sim 10^{-4} L_{star}$ (Rebull et al. 2008), which makes the most luminous circumstellar discs in Cha-I $\sim 10^3$ times more luminous than these debris discs and therefore clearly primordial. This is also not taking into account any contribution to the disc luminosity in the NIR regime.

The observed luminosities were compared with values obtained from our simple model (see Appendix C1), for different inclination angles, $i = 0°, 70°$. SY Cha as a template for the stellar parameters, as it appears to be a typical Class II source, see Fig 3 (b). These model luminosities are overplotted in Figs. 7 (a) - (b). It is evident that the scatter in our luminosity plots is larger than expected from variation of the inclination angle. The scatter expected from 78% of our objects should be half an order of magnitude but we have at least an order of magnitude scatter in our plots. This indicates that additional factors, such as dust settling, must be contributing to the diversity as already pointed out in Section 4.

6 DISC MASSES

One of the main benefits of the submm/mm regime for studies of discs is that the dust becomes optically thin, so it is possible to infer the total amount of dust in the disc. In the following we will explore the possibility of calculating disc masses for the sample of discs in Cha-I using Herschel data.

6.1 Testing 'monochromatic' disc masses

Disc masses of a large number of objects are often computed from single wavelength sub-mm and/or mm fluxes. It is assumed that the emission is optically thin and that a single temperature (typically ~ 20 K) can be assumed to describe the emission of the whole disc (Hildebrand 1983; Beckwith et al. 1990):

$$M_d = \frac{D^2 F_\nu}{\kappa_\nu B_\nu(T_c)} \qquad (4)$$

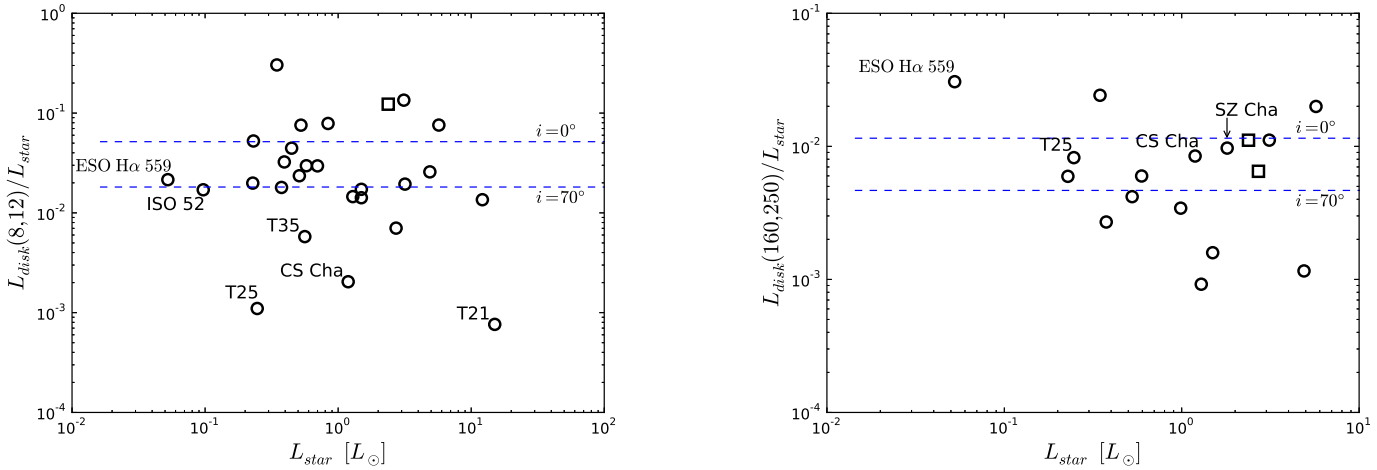

(a) (b)

Figure 7. Luminosity plots with symbols as in Fig. 4. The blue dotted lines are the flux density values for a typical Class II obtained from the simple model (see Appendix C1) for different angles of inclination: $i = 0°, 70°$.

Here D is the distance to the star, κ_ν is the opacity, F_ν is the flux density and $B_\nu(T_c)$ is the Planck function at a characteristic temperature T_c.

Disc masses calculated from this simple scaling law are called 'monochromatic' masses in the following. So far, most surveys of disc masses have been carried on at 850 μm or 1.3 mm. The availability of the Herschel surveys of star-forming regions at shorter wavelengths (70-500 μm) raises the question of how suitable these wavelengths are for estimating disc masses.

This question is addressed by using 8 objects as test cases in the sample. For these objects both Herschel data and measurements of fluxes at longer wavelengths, either 850 or 1300 μm, were available. The FIR/submm/mm SED of these objects is modelled with the simple model described in Appendix C1 for the stellar parameters listed in Table A1. For each object a value of the disc mass,M_d, is derived. A fit of the SED is not carried out. Instead, the parameters of the model were varied within the plausible ranges until a satisfactory by-eye match was achieved. Note that we did not attempt to fit the NIR and MIR fluxes as this part of the SED does not affect the disc mass. In all 8 cases, a well-matched model is found with disc masses between 0.002 and 0.05 $M_\odot$, called the 'true' disc masses in the following.

These 'true' masses (M_d) are compared to the monochromatic disc masses ($M_d(\lambda)$) obtained from single-wavelength fluxes following Eq. 4. For the monochromatic masses, we adopt the same opacity law as for the true masses with $\beta = 1.0$ and $\kappa_{f=230\mathrm{GHz}} = 0.023\,\mathrm{cm}^2\ \mathrm{g}^{-1}$ (see Appendix C1). We also adopt a temperature of $T_c = 20\,\mathrm{K}$, a distance of $D = 160\,\mathrm{pc}$, and a dust-to-gas ratio of 1:100. These parameters are chosen to be both plausible and easily comparable with a wide range of literature surveys (see for example Beckwith et al. (1990); Shirley et al. (2000); Andrews & Williams (2005); Scholz et al. (2006); Ricci et al. (2010); Lee et al. (2011)).

The results of this comparison are shown in Fig. 8, which plots the ratio of monochromatic vs. the 'true' disc mass as a function of wavelength for each of the 8 objects. One can see that in most cases the monochromatic masses in the FIR and submm regime are all within a factor of 3 of the 'true' values from modeling, which we consider to be the typical uncertainty in disc masses. The deviations are straightforward to explain with scatter in the opacity and in the dust temperature, which are the main sources of uncertainty. Adopting a different temperature in the range 20-30 K does not significantly change this result. However, we note that using a single temperature for a sample spanning a large range of stellar luminosities may introduce a systematic effect as it tends to underestimate the disc mass at low luminosity and overestimate it at high luminosity. Our sample is skewed toward high luminosity objects, and does not allow us to further explore this effect. We conclude that fluxes at the Herschel wavelengths 160-500 μm can be used to estimate robust disc masses for large samples without detailed modeling.

Kim et al. (2009) calculate monochromatic disc masses for 5 of our objects (all TDs), based on 1.3 mm fluxes. They use almost the same dust opacity ($0.02\,\mathrm{cm}^2\ \mathrm{g}^{-1}$ at 1.3 mm), but a significantly higher temperature of $T_c = 50\,\mathrm{K}$. These seems unrealistic; using our model, we obtain significantly lower temperatures for the outer regions of the discs. Still, their monochromatic values agree with ours within a factor of three.[2]. For one of our objects, ESO Ha 559, Olofsson et al. (2013) determine a disc mass from radiative transfer modeling and a specified grain size distribution. Their result of 0.005 $M_\odot$ is very similar to ours (0.0055 $M_\odot$).

[2] Note that for three out of these five, T21, T25 and T35, Kim et al. (2009) actually use upper flux limits at 1.3 mm from Henning et al. (1993), but the resulting disc masses are not listed as upper limits

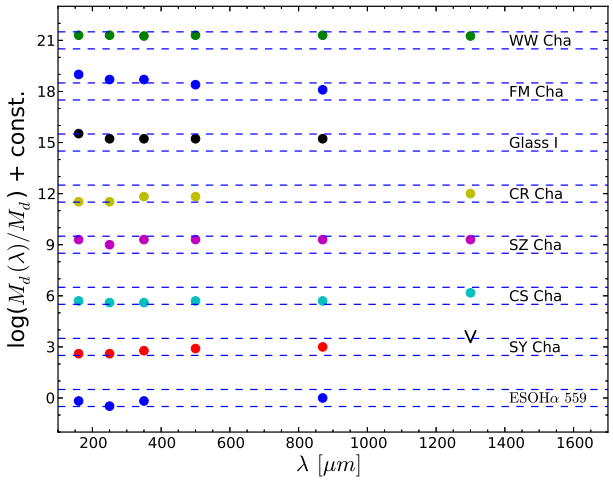

Figure 8. Ratio of monochromatic disc masses, $M_d(\lambda)$, to 'true' disc masses, M_d, from SED fitting for 8 objects in Cha-I, as a function of wavelength. Each object is shifted vertically and labelled; the dashed lines show in each case the interval ± 0.5 dex around $M_d(\lambda)/M_d = 1$. The objects are plotted in order of increasing luminosity. '$\vee$' represents a disc mass calculated using a flux density upper limit.

6.2 Disc Masses

Having established that Herschel fluxes at $\geqslant 160\,\mu$m can be utilized to estimate disc masses, we have used Eq. 4 to calculate monochromatic disc masses for all objects with at least one flux measurement at 160-500 μm, excluding the Class I sources which may be affected by emission from the envelope. The results are given in Table 2. In the last column, we also list the average disc masses for the Herschel wavelengths; these averages are adopted for the following analysis. Based on the evaluation in Section 6.1, the typical uncertainty in these values is a factor of 3. In total, disc masses were obtained for 34 objects, the largest sample of disc masses for the Cha-I region published thus far, about twice as many as in Henning et al. (1993).

This sample can be used to study the overall distribution of disc masses in Cha-I. The histogram of the 34 values in our sample is shown in Fig. 9. The disc masses range from 10^{-3} to $10^{-1}\,M_\odot$, with a median of $0.005\,M_\odot$ for Class IIs. This number is similar to the median disc mass found for Class IIs in the coeval regions Taurus ($0.003\,M_\odot$, Andrews & Williams (2005)), ρ Oph ($0.005\,M_\odot$, Andrews & Williams (2007) and IC348 ($0.002\,M_\odot$, Lee et al. (2011)), although the samples are not fully comparable due to different selection effects and methods. We stress again that our sample only covers the most luminous discs in Cha-I, i.e. the median value should be interpreted as an upper limit. We also note that the scatter in disc masses is 2-3 orders of magnitude and thus significantly larger than the uncertainty, a clear sign of dispersion in the dust content in an approximately coeval population of young discs.

However, TDs do not have on average lower or higher disc masses than the rest of the sample. The median disc mass for the objects classed in Section 4 as TDs is $0.006\,M_\odot$.

Andrews et al. (2011) studied a sample of 12 TDs from different star-forming regions. They found that their sample of TDs had similar disc masses to the Class IIs in Ophiuchus (Andrews et al. 2010). This agrees with what we have found for Cha-I. In contrast to this, Najita et al. (2007) found that for a sample of 12 TDs from Taurus the median disc mass for TDs was 4 times larger than for the Class IIs in Taurus. All these TD samples are relatively small, and the selection criteria differ. It is therefore not clear whether the difference in the results bears any statistical significance.

Only two objects in our sample have disc masses clearly above the 'Minimum Mass Solar Nebula' (MMSN) of around $0.02\,M_\odot$, which corresponds to the mass of gas and dust required to make the solar system planets (Davis 2005). A handful more are around this limit. Since we are sampling the most luminous discs in this region and the total number of stars with discs in Cha-I is around 100 (Luhman et al. 2008), the fraction of objects with MMSN discs is between 2 and 7%, consistent with what has been estimated by Greaves & Rice (2010) based on the earlier survey by Henning et al. (1993). Contrasted with the abundance of exoplanetary systems with massive planets, our results confirm the 'missing mass' problem stated by Greaves & Rice (2010) and suggests that the majority of these discs will either never form Jupiter-mass planets or that the formation of larger bodies is already well underway. We note that most of the disc surveys collated by Greaves & Rice (2010) use a mm dust opacity similar to the one adopted by us.

We use the Herschel disc masses to probe the relation between disc and stellar mass. For this purpose, we remove 5 objects without known stellar parameters (4 of them are classified as 'flat spectrum'). All remaining sources are either Class II or TDs. We estimate stellar masses for this sample by comparing the effective temperatures with a 3 Myr isochrone from Siess et al. (2000).[3] This isochrone was found to reproduce the trend seen in the HR diagram and thus represents a good approximation for our sample. The disc masses are plotted vs. stellar masses in Fig. 10.

At first glance, the figure may indicate a trend of larger disc masses towards higher mass objects. However, we found no statistically significant correlation between disc masses and stellar masses, using various correlation tests (linear regression, Rank correlation test). Given the large scatter, the relatively small number of datapoints, and the relatively small range in masses this is not surprising. Previous studies who have found such trends (most notably, the recent paper by Andrews et al. (2013)) covered at least two orders of magnitude in stellar mass, whereas our sample is limited to one order of magnitude.

In terms of relative disc masses ($M_d/M_\star$), the median in our sample is 0.5%, which is consistent with previous studies in Taurus and ρ Ophiuchus (Mohanty et al. 2013; Andrews & Williams 2007; Andrews et al. 2013). This indicates that the disc evolution in these four regions is progressing on similar timescales, without strong environmental difference.

[3] `http://www.astro.ulb.ac.be/~siess/WWWTools/Isochrones`

Table 2. Monochromatic disc masses derived from the Herschel fluxes and their average for objects in Cha-I. All values are in $M_\odot$. See text for details.

2MASS Coordinate Identifier	Other Identifier	M_{star} $[M_\odot]$	M_d ($M_\odot$) 160 [μm]	250 [μm]	350 [μm]	500 [μm]	Average
J10563044-7711393	SY Cha	0.5	0.004	0.004	0.006	0.008	0.006
J10581677-7717170	SZ Cha	2.2	0.02	0.01	0.02	0.02	0.02
J10590699-7701403	CR Cha	1.9	0.01	0.01	0.02	0.02	0.02
J11022491-7733357	CS Cha	1.0	0.01	0.008	0.008	0.01	0.01
J11040909-7627193	CT Cha	1.1	0.004	0.003	0.004	0.004	0.004
J11061540-7721567	T21	2.5	0.04	–	–	–	0.04
J11062554-7633418	ESO Hα 559	0.2	0.002	0.001	0.002	–	0.002
J11070919-7723049	Ced110-IRS4	–	0.03	0.02	0.03	0.06	0.03
J11071206-7632232	UZ Cha	0.5	0.001	0.0007	–	–	0.0009
J11071622-7723068	ISO97	–	0.009	0.009	–	0.006	0.008
J11071915-7603048	T25	0.4	0.002	0.001	0.002	–	0.002
J11072074-7738073	DI Cha	2.5	0.008	–	–	–	0.008
J11072142-7722117	B35	–	0.002	–	–	0.008	0.005
J11074366-7739411	FI Cha	0.6	0.002	0.003	–	–	0.003
J11075792-7738449	FK Cha	0.9	0.03	0.02	0.02	–	0.02
J11080148-7742288	VW Cha	0.7	0.003	–	–	–	0.003
J11080297-7738425	ISO126	0.4	0.009	0.008	0.003	–	0.007
J11081509-7733531	Glass I	2.5	0.02	0.01	0.01	0.01	0.01
J11083905-7716042	T35	0.7	0.001	–	–	–	0.001
J11092266-7634320	C1-6	0.5	0.003	–	–	–	0.003
J11092379-7623207	VZ Cha	0.9	0.002	0.002	0.003	0.006	0.003
J11094192-7634584	C1-25	–	0.01	–	0.001	0.02	0.01
J11094742-7726290	B43	0.3	0.001	0.002	0.003	0.004	0.003
J11095340-7634255	FM Cha	1.1	0.04	0.02	0.02	0.01	0.02
J11095407-7629253	Sz33	0.4	0.002	–	–	–	0.002
J11095505-7632409	C1-2	–	0.01	–	–	–	0.01
J11095873-7737088	WX Cha	0.5	0.001	–	–	–	0.001
J11100010-7634578	WW Cha	1.1	0.1	0.1	0.09	0.1	0.1
J11100369-7633291	Hn11	0.7	0.005	–	–	–	0.005
J11100704-7629376	WY Cha	0.6	0.0006	–	–	–	0.0006
J11104959-7717517	HM27	0.4	0.002	–	–	–	0.002
J11113965-7620152	XX Cha	0.4	–	0.0007	0.001	–	0.0009
J11114632-7620092	CHX 18N	0.9	0.001	0.001	0.001	–	0.001
J11122772-7644223	CV Cha	2.5	0.007	0.004	0.003	0.004	0.004

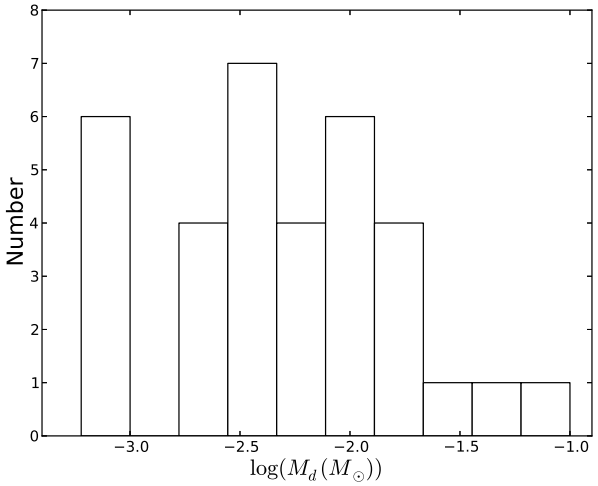

Figure 9. Histogram of the monochromatic disc masses calculated using the Herschel fluxes, see Section 6.2.

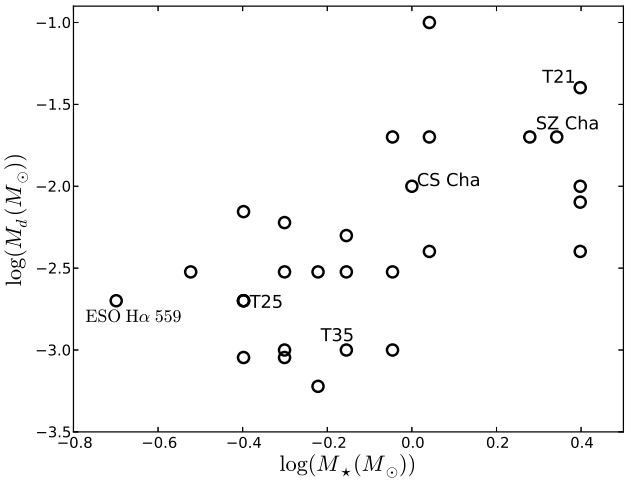

Figure 10. Disc masses in Cha-I plotted against stellar masses: with symbols as in Fig. 4. See text for details.

7 TRANSITION DISCS

In the following section we briefly discuss the subsample of TDs, i.e. the objects with evidence for some degree of dust clearing in the inner disc which separates them from the Class IIs in Fig. 4 and Fig. 5. We consider here 7 objects with evidence of a deficit of an emission in the NIR/MIR and a rise in the SED between 10 and 20 μm.

We use the simple model described in Appendix C1 to describe the SEDs of the TDs, specifically, to obtain values for the inner radius of the disc. To create an SED of a TD using this model we merely set the first value of r in Eq. C2 to be much larger than r_0 and we called this initial value r_{td}, whereas for a normal Class II source the first value of r is equal to r_0. We varied r_{td} until our model matched the increase in flux density around 10-20 μm. Then we varied T_0, q, β, R_d and i from their initial fiducial values mentioned in Appendix C1 to fit the rest of the SED. We kept within the ranges that are considered to be reasonable for these parameters, which are given in Appendix C1. Note that this model does not allow us to fit the silicate feature or any other excess emission bluewards of the steep increase in flux density.

The SEDs with the matching model are shown in Fig. 11; their parameters are listed in Table 3. Note that the SED for T21 is instead given in Fig. 3 (c). In particular, we found values for r_{td} ranging from 0.185 - 13.3 AU. The SEDs reveal a large diversity of features which reflects the variety of physical conditions and geometry of the TDs. Four objects out of 7, Figs. 11 (c),(d),(f) and Fig. 3 (c) are well matched by our simple model from 10 μm onwards. For the other 3 objects, however, Figs. 11 (a),(b),(e), the simple model underestimates the flux density between 10 - 70 μm. For these objects which are poorly matched by our model the assumptions made in our approach are probably not suitable.

Kim et al. (2009) model 5 out of the 7 TDs that we have investigated. The inner radii that they obtained are also shown in Table 3; they range from 8.1 - 146.7 AU and are about an order of magnitude larger than ours. This discrepancy is a result of the different assumptions made when modeling the SED. In our simple model, we consider the dusty disc to be truncated, without any further modification at the inner edge of the disc. We assume that the inner edge of the disc is not directly irradiated by the star. On the other hand, Kim et al. (2009) (in line with other authors, e.g. D'Alessio et al. (2005); Espaillat et al. (2007a); Brown et al. (2007); Espaillat et al. (2007b)) use more complex models which assume that the inner edge of the outer optically thick disc is directly exposed to the stellar radiation. As a consequence, a so-called wall will develop. Since the rise in the SED essentially constrains the maximum temperature of the optically thick disc, assuming that the edge of the disc is directly exposed to the stellar radiation makes it hotter; therefore the same temperature is reached further out from the star, i.e. r_{td} is increased. Thus, the difference between our results and the ones from Kim et al. (2009) is as expected.

It is clear that neither of these models is entirely correct as some amount of gas and dust inside the inner cavity is observed in most TDs. Most of the TDs in our sample show some level of excess emission in the NIR and MIR bluewards of the rise in the SED (see Fig. 11), indicating the presence of dust in the cavity. Moreover, two of the TDs have quite high accretion rates of $\sim 10^{-8}\,M_\odot$ yr^{-1} (Antoniucci et al. 2011), see Table A1. This means that gas is also present near the central object. The effect of this material on the location and development of an inner wall needs to be addressed using more realistic 2D models. Here we are merely stressing the very large uncertainty that any simple assumption will have on the determination of r_{td} from the SED.

Resolved imaging of the gaps in the discs is only available for one of the objects discussed here. Cieza et al. (2013) use Sparse Aperature Masking (SAM) to investigate T35. They find an inner disc, a gap and then an outer disc, with its inner edge at ∼8.3 AU. Using submm interferometry, Cieza et al. (2013) find 8.1 AU cavity radius for the same object. These results are approximately an order of magnitude larger than our r_{td} inferred from the SED (0.95 AU). More indirect constraints can be gained by looking for stellar companions. If a companion is detected within the disc, the cavity radius has to be at least as large as the distance between object and companion. While all our TDs have been observed with resolution of $\sim 0\farcs1$ (corresponding to $\sim$ 15 AU), either with Adaptive Optics at the VLT (Lafrenière et al. 2008) or with the HST (Robberto et al. 2012), only two of them have a confirmed companion. SZ Cha has a wide companion at 800 AU, i.e. presumably outside the disc. T21 has a companion at $\sim$ 22 AU, about twice as large as our estimate for r_{td}. Thus, for two of our objects, T21 and T35, our values for r_{td} are too small, indicating the necessity of considering more complex models, possibly the inclusion of a wall-like feature. Note that these two are well approximated by our simple model (see Fig. 11).

Based on the observational parameters, we can speculate about the possible origins of the cavities in the TDs in Cha-I. In general, photoevaporation models for TDs predict low accretion rates, small inner hole sizes and low disc masses (Alexander & Armitage 2007; Owen et al. 2011).The known accretion rates for our sample are most likely too high for photoevaporation scenarios. In addition, most of the disc masses estimated for our sample are relatively large compared with the predictions for photoevaporation. Thus, alternative scenarios need to be considered. The presence of close-in companions or massive planets inside the gaps is a plausible option for the majority of these TDs.

8 SUMMARY AND CONCLUSIONS

We have carried out a multi-wavelength study of circumstellar discs around 44 YSOs in the Cha-I star-forming region. In particular we made use of the recent release of Herschel data for Cha-I. For a sample of 8 test cases (all of which have either a sub-mm or mm flux measurement) we examined whether Herschel fluxes at a single wavelength could be used to derive disk masses (monochromatic masses). We found that Herschel fluxes at 160-500 μm can be used to derive robust estimates of the disc mass. In most cases the monochromatic masses in the FIR and submm regime are within a factor of 3 of the 'true' values from modeling. The deviations can be explained by a scatter in the opacity and in the dust temperature, which are the main sources of uncertainty.

Table 3. Derived properties of TDs in Cha I using the simple model from Appendix C1

2MASS Coordinates	Name	q	β	r_{td} [AU]	$r_{\rm Kim}^{a}$ [AU]	T(r_{td}) [K]	T($r_{\rm Kim}$) ^{b} [K]	R_d [AU]	i	M_d [$M_\odot$]
J10581677−7717170	SZ Cha	0.49	0.6	1.10	29.5	195	90	100	60°	0.015
J11022491−7733357	CS Cha	0.54	0.3	2.2	41.1	127	62	150	0°	0.02
J11044258−7741571	ISO 52	0.59	0.8	0.185	-	216	-	100	50°	< 0.0003
J11061540−7721567	T21/Ced 110 IRS 2	0.58	1.0	13.3	146.7	56	66	150	0°	0.03
J11062554−7633418	ESO Hα 559	0.55	0.9	0.4	-	193	-	100	55°	0.0055
J11071915−7603048	T25	0.57	1.2	1.0	8.1	132	90	150	50°	0.002
J11083905−7716042	T35/FL Cha	0.6	0.3	0.95	15.2	137	80	100	40°	0.002

^{a} $r_{\rm Kim}$ is r_{td} as calculated by Kim et al. (2009), ^{b} T($r_{\rm Kim}$) is the temperature at r_{td} calculated by Kim et al. (2009)

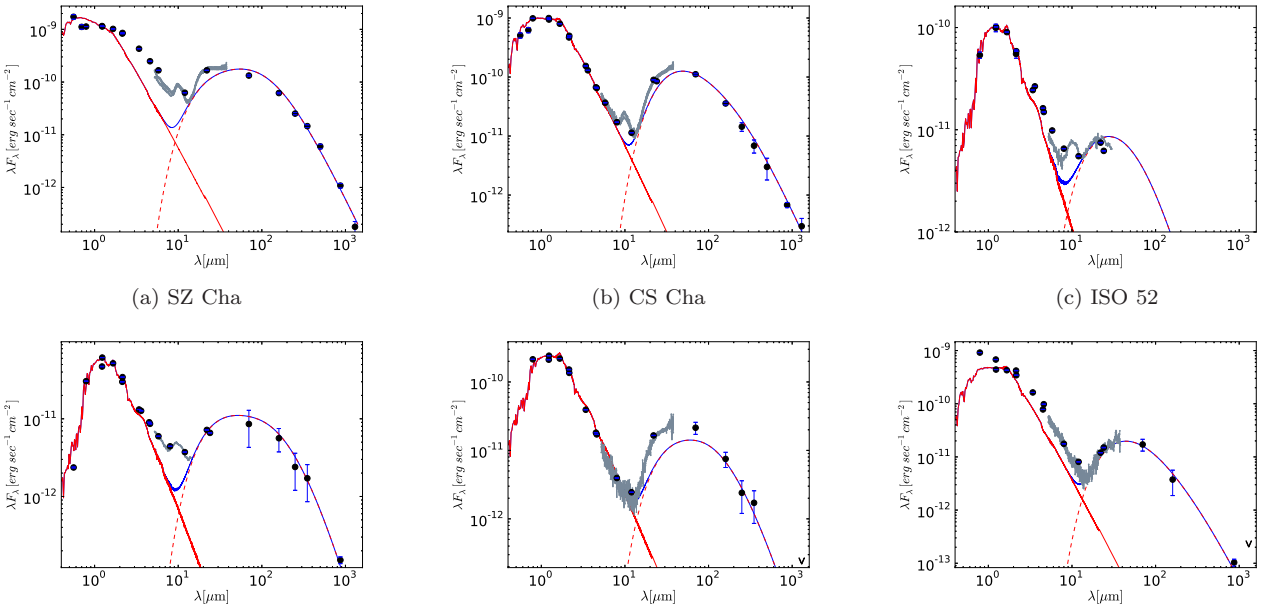

(a) SZ Cha (b) CS Cha (c) ISO 52

(d) ESO Hα 559 (e) T25 (f) T35

Figure 11. SEDs of TDs fitted using the simple model (see Appendix C1). The red line is the model atmosphere, the dotted red line is the simple model fit and the blue line is combination of both.

In total, disc masses were obtained for 34 objects, the largest sample of disc masses published thus far for the Cha-I region, about twice as many as in Henning et al. (1993). The median disc mass is 0.005 $M_\odot$ for Class IIs, corresponding to on average 0.5% of the stellar mass, but with a scatter of 2-3 orders of magnitude. The median disc mass for TDs is 0.006 $M_\odot$. The fraction of objects in Cha-I with at least the 'minimum mass solar nebula' is only 2-7%. These numbers are consistent with previously published results in other regions (Taurus, IC348, ρ Oph).

Diagrams of spectral slopes, making use of Herschel data, show the effect of specific evolutionary processes in circumstellar discs. We found that in our sample of objects the Class IIs show a wide scatter in the α_{K-70} spectral slope. We ascertained using a 2-layer disc model that this scatter can be explained as a consequence of dust settling. We found that there is a similar scatter in the α_{K-70} spectral slope for TDs. We identify a continuous trend from Class II to TDs which can be accounted for by assuming inner disc clearing. We discuss the implications of simple assumptions for the determination of the inner gap radius from SED fitting. The development of an inner wall needs to be addressed using more realistic 2D models.

Including Herschel fluxes in this type of analysis highlights the diversity of TDs. We find that TDs do not show any significant difference compared with Class IIs in terms of far-infrared luminosity, disc mass, or amount of dust settling. Taken together, this indicates that inner dust clearing occurs independently from other evolutionary processes in the discs.

ACKNOWLEDGMENTS

We would like to thank the anonymous referee for helpful comments which improved the manuscript.

Table A1. Derived properties for our 44 objects in Cha I from Luhman (2007) and accretion rates from Antoniucci et al. (2011); Costigan et al. (2012).

Coordinate identifier	Other identifier	Evol. class	Spectral Type	$T_{\rm eff}$ [K]	A_J -	L_{star} [$L_\odot$]	$\dot{M}$ [a] [$\dot{M}_\odot$ yr^{-1}]	$\dot{M}$ [b] [$\dot{M}_\odot$ yr^{-1}]
J10563044-7711393	SY Cha, T4, Sz3	II	M0.5	3778	0.23	0.57	-	
J10581677-7717170	SZ Cha, T6	II/TD	K0	5250	0.42	1.9	-	
J10590699-7701404	CR Cha, T8, Sz6	II	K2	4900	0.00	2.4	-	
J11022491-7733357	CS Cha, T11	TD	K6	4205	0.07	1.2	1.96×10^{-08}	
J11040909-7627193	CT Cha, T14	II	K5	4350	0.45	0.95	1.42×10^{-08}	
J11042275-7718080	HH48, T14A	I	K7	4060	0.45	0.013	-	
J11044258-7741571	ISO52	II	M4	3270	0.36	0.093	1.17×10^{-09}	
J11061540-7721567	Ced110-IRS2, T21	III	G5	5770	0.92	16	-	
J11062554-7633418	ESO Ha 559	II	M5.25	3091	1.01	0.052	-	
J11063460-7723340	Cha MMS-1	0	-	-	-	-	-	
J11064658-7722325	Ced110-IRS4	I	-	-	-	-	-	
J11070919-7723049	Ced110-IRS6	Flat	-	-	-	-	-	
J11071206-7632232	UZ Cha, T24	II	M0.5	3778	0.63	0.36	-	
J11071622-7723068	ISO97	Flat	-	-	-	-	-	
J11071915-7603048	T25, Sz18	II	M2.5	3488	0.45	0.24	-	
J11072074-7738073	DI Cha, T26	II	G2	5860	0.75	12	5.98×10^{-08}	6.9×10^{-8}
J11072142-7722117	B35	Flat	-	-	-	-	-	
J11074366-7739411	FI Cha	II	M0	3850	1.35	1.4	-	
J11075730-7717262	CHXR30b	II	M1.25	3669	3.16	0.22	7.72×10^{-09}	
J11075792-7738449	FK Cha, HM16	Flat	K6	4205	1.24	2.4	-	
J11080148-7742288	VW Cha, T31	II	K8	3955	0.72	3.0	1.67×10^{-07}	8.71×10^{-8}
J11080297-7738425	ISO126	II	M1.25	3669	1.35	0.33		2.23×10^{-9}
J11081509-7733531	Glass I, T33A	Flat	G7	5630	0.85	2.8	-	
J11083896-7743513	IRN	I	-	-	-	-	-	
J11083905-7716042	T35, ISO151	II	K8	3955	1.31	0.53	-	
J11085464-7702129	VY Cha, T38, Sz29	II	M0.5	3778	0.90	0.34	7.13×10^{-09}	
J11091812-7630292	CHXR79, Hn9	II	M1.25	3669	1.92	0.55	1.58×10^{-08}	
J11092266-7634320	C1-6, P30	II	M1.25	3669	3.27	0.80	4.74×10^{-08}	
J11092379-7623207	VZ Cha, T40	II	K6	4205	0.56	0.53	-	
J11092855-7633281	ISO192	I	-	-	-	-	-	
J11094192-7634584	C1-25, ISO199	II	-	-	-	-	-	
J11094742-7726290	B43, ISO207	II	M3.25	3379	2.26	0.22	2.36×10^{-08}	4.07×10^{-9}
J11095340-7634255	FM Cha, HM23	II	K5	4350	1.47	3.0	1.42×10^{-07}	
J11095407-7629253	Sz33, T43	II	M2	3560	1.47	0.48	1.63×10^{-08}	
J11095505-7632409	C1-2, ISO226	Flat	-	-	-	-	-	
J11095873-7737088	WX Cha, T45	II	M1.25	3669	0.56	0.84		1.51×10^{-8}
J11100010-7634578	WW Cha, T44	II	K5	4350	1.35	5.5	-	
J11100369-7633291	Hn11, ISO232	II	K8	3955	2.14	0.66	-	
J11100704-7629376	WY Cha, T46	II	M0	3850	1.13	1.4	-	
J11103801-7732399	CHXR47	II	K3	4730	1.44	2.6		
J11104959-7717517	HM27, T47	II	M2	3560	1.17	0.42	1.41×10^{-08}	
J11113965-7620152	XX Cha, T49, Sz39	II	M2	3560	0.34	0.37	1.55×10^{-08}	
J11114632-7620092	CHX 18N, Cam1-103	II	K6	4205	0.20	1.3	-	
J11122772-7644223	CV Cha, T52	II	G9	5410	0.42	5.0	-	

[a] Antoniucci et al. (2011), [b] Costigan et al. (2012)

APPENDIX A: LIST OF PROPERTIES FOR OBJECTS

In Table A1 we list the entire sample considered in this paper, including stellar parameters, evolutionary classes, and accretion rates collected from the literature.

APPENDIX B: COMMENTS ON PECULIAR OBJECTS

As already mentioned in Section 3.2 we exclude T54 from the sample as it suffers from extended source contamination (Matrà et al. 2012).

B1 Candidate edge-on discs

We discuss briefly 3 objects that may be edge-on discs. ESO Hα 569 and ESO Hα 559 appear to be TDs, based on their SEDs. We are interested in the characteristics of TDs, hence it is important for us to clarify whether or not we consider them to be TDs or edge-on discs. Lastly, HH48/T14A is also potentially an edge-on disc. It is class I, from examination of the SED, so it does not affect our TD sample. The SEDs for these objects are given in Fig. B2.

B1.1 ESO Hα 569

Robberto et al. (2012) found ESO Hα 569 to be a nearly edge-on disc with an angle of inclination of 87.1° using the online SED fitting tool from Robitaille et al. (2006). We found a best fit of 81.4° using the online SED fitting tool, even when we included the *Herschel* data which were not available before. Including the LABOCA data point gave a best fit of 18.2°. Luhman (2007) state that the absence of a detection of this star in the X-ray images from Feigelson & Lawson (2004) can be used to constrain the amount of extinction towards the star, indicating an extinction of $A_K \gtrsim 60$ towards this star. This high extinction and the underluminosity of the object in the HR diagram, see Fig. 2, support the conclusion that ESO Hα 569 is an edge-on disc. This object is not mentioned in Ribas et al. (2013) but is included in Winston et al. (2012). In the recent study by Olofsson et al. (2013) it was also concluded that this object is a likely edge-on disc, based on modeling the infrared SED.

B1.2 ESO Hα 559

There are two reasons why this object has previously been classed as edge-on disc. First, ESO Hα 559 was found by Robberto et al. (2012) to be a nearly edge-on disc using the online SED fitting tool from Robitaille et al. (2006). We attempted to reproduce the results by Robberto et al. (2012) using the same tool, but could not fit the observed *Herschel* flux densities for ESO Hα 559.

Second, Ribas et al. (2013) state that the underluminosity of ESO Hα 559 with respect to its spectral type also supports this scenario. But ESO Hα 559 is not underluminous in the HR diagram, see Fig. 2, and so we see no reason to classify it as a nearly edge-on disc.

B1.3 HH48/T14A

HH48 is a class I source which is underluminous in the HR diagram. Luhman (2004) suggests that HH48 is underluminous because it is an edge-on disc. There is no further information available to suggest that this is indeed the case. In the absence of further information the question remains open. The SED of HH48/T14A is class I and there is no evicence for inner disk clearing or dust settling, i.e. for the purposes of this work it is immaterial whether the object is edge-on or not.

B1.4 ISO 237 and Hn10e

Manoj et al. (2011), using Spitzer data, report that ISO 237 had a problem with source contamination. They also report that Hn10e suffered from contamination from a nearby bright object. It is probable that they are also contaminated in the Herschel bands. We exclude ISO 237 and Hn10e from our sample, their SEDs are shown in Fig. B1. Kim et al. (2009); Ribas et al. (2013) do not consider these objects.

APPENDIX C: VARIABLE SOURCES

For 7 objects, the photospheric model deviates strongly from some of the optical and NIR datapoints. Since the photometry used to compile the SED spans several decades, the most likely reason for this discrepancy is variability. Whereas long-term red and NIR variations of up to 20% are common in young stellar objects, objects with more variability are rare (Scholz 2012).

To test the variability hypothesis, we obtained new and simultaneous multi-band images for the 7 objects that we could not fit with the photospheric SED. For this purpose we used the dual-channel imager 'Andicam' at the 1.3m telescope on Cerro Tololo. The data was taken in the framework of the SMARTS project DUBLIN-13A-0001 (PI: A. Scholz) over several nights in May 2013.

For all 7 objects we obtained optical images in the R and I bands (3 × 110 s exposures) and NIR images in the J and K bands (5 × 30 s in a five-position dither pattern). A standard reduction was carried out including flatfield and bias correction, plus sky subtraction for the NIR data. The magnitudes were measured using aperture photometry. The NIR magnitudes were shifted into the 2MASS system using a few (2-5) other stars in the same field of view. The optical magnitudes were shifted into the Landolt system using standard star images taken in the same night and at similar airmass. The photometry for these 7 objects is listed in Table C1, in comparison with 2MASS and DENIS magnitudes.

All of them show evidence for variability, which explains the poor fit of the photospheric SEDs. For some of them, the new measurements mostly agree with the DENIS magnitudes, but the 2MASS photometry is inconsistent (see no. 1, 2 or 4 in the table), possibly indicating a short-term event like an eclipse or a burst. One more object (no. 6) has only one major outlier in the DENIS measurements. One star (no. 3) varies within a range of 0.2 mag in J, but 0.7 mag in K, indicating that the variability arises in the disc. The remaining two sources (5 and 7) show drastic variations in the J-band (2.3 and 1 mag), but smaller changes in the K-band (1.2 and 0.4 mag), i.e. the amplitudes in the J-band are by a factor of ~ 2 larger than in the K-band, which can be explained by the presence of accretion-related hot spots or variable extinction along the line of sight (Scholz et al. 2009). For a more detailed assessment of the causes of the variability, continuous monitoring in multiple bands is required.

C1 Description of Simple Disc Model

The simplest way to model a circumstellar disc is to assume it emits as a series of blackbodies. The model that we used, as in Beckwith et al. (1990), treats the disc as geometrically thin in the vertical direction. In the radial direction the disc is modelled as a number of concentric rings of dust starting at an inner radius r_0 up to an outer radius of R_d. This model can reproduce the main features of a SED for a class II source. It is assumed that the dust grains in the disc are predominantly of the same kind and are in thermal equilibrium. The flux density, at frequency ν, is then given by

$$F(\nu) = \frac{cos(i)}{D^2} \int_{r_0}^{R_d} B_\nu(T(r)) \left(1 - e^{-\tau_\nu}\right) 2\pi r \, \mathrm{d}r, \qquad \text{(C1)}$$

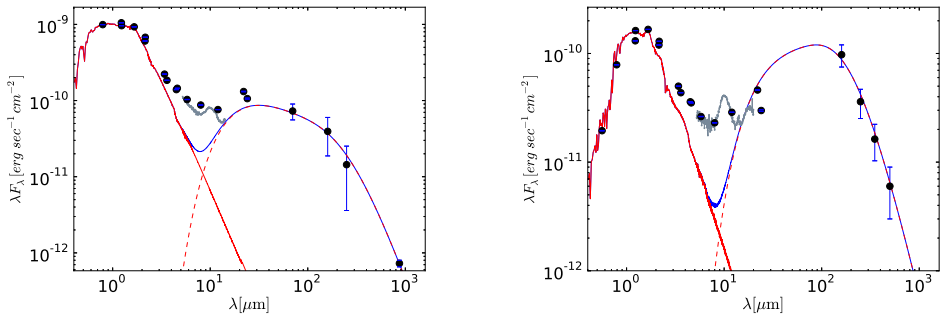

(a) ISO 237 (b) Hn10e

Figure B1. SEDs of objects potentially suffering from contamination which are excluded from our sample.

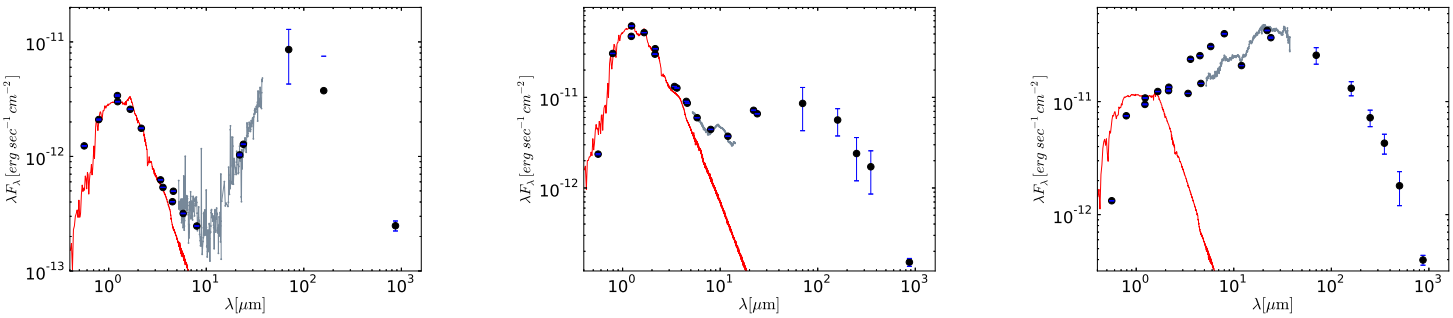

(a) ESO Hα 569 (b) ESO Hα 559 (c) HH48

Figure B2. SEDs of outliers in HR diagram and potential edge-on discs.

where $T(r)$ is the temperature of the disc at radius r, $B(T_\nu)$ is the Planck function for frequency ν and τ_ν is the optical depth at distance r from the centre of the star for frequency ν. D is the distance to the star from the observer which is taken to be $D = 160\,\mathrm{pc}$, i is the angle of inclination of the disc where 90° is edge on. This model fails for high angles of inclination, $i \gtrsim 80°$, and more sophisticated models are needed, see Chiang & Goldreich (1999).

The temperature and surface density profiles that we adopt are simple power laws, given by:

$$T(r) = T_0 \left(\frac{r}{r_0}\right)^{-q}, \qquad \Sigma(r) = \Sigma_0 \left(\frac{r}{r_0}\right)^{-p} \tag{C2}$$

where T_0 and Σ_0 are the values at r_0. The disc mass is given by

$$M_d = \int_{r_0}^{R_d} \Sigma(r) 2\pi r dr \tag{C3}$$

We can express the surface density at r_0, Σ_0, in terms of M_d by combining Eqs. C2, C3:

$$\Sigma_0 = \frac{M_d(2-p)}{2\pi r_0^p}(R_d^{2-p} - r_0^{2-p})^{-1} \tag{C4}$$

The opacity and the optical depth are given by:

$$\kappa_\nu = \kappa_f \left(\frac{\nu}{\nu_f}\right)^\beta, \qquad \tau_\nu(r) = \frac{\kappa_\nu}{cos\ i}\Sigma(r) \tag{C5}$$

The initial values that we use are $p = 1.5$, $\beta = 1.0$, $q = 0.58$, $r_0 = 5R_{star}$, $R_d = 200\,\mathrm{AU}$ and $\kappa_{f=230\mathrm{GHz}} = 0.023\,\mathrm{cm^2\ g^{-1}}$. We used $T_0 \approx 880(T_*/4000)\,\mathrm{K}$ following the reasoning of Mohanty et al. (2013) and Andrews & Williams (2005), but with an upper limit at $\sim 1000\,\mathrm{K}$. These are the fiducial parameters used in Section 4.

When trying to reproduce observed SEDs (Sections 6 and 7), some of these parameters were changed within a plausible range. We took $0.0001 M_\odot \lesssim M_d \lesssim 0.1 M_\odot$ to be a reasonable range in disc mass, and $50 \lesssim R_d \lesssim 200\,\mathrm{AU}$ for the outer disc radius. We assumed that $0.4 \lesssim q \lesssim 0.6$ which is roughly the range given by radiative transfer models (Chiang & Goldreich 1997; D'Alessio et al. 1998) and $0 \lesssim \beta \lesssim 2$ based on observational constraints (Ricci et al. 2010). The parameter p was varied in the range $0.5 < p < 1.5$. We avoided using $i \gtrsim 80°$, for the reason mentioned above.

REFERENCES

Adams F. C., Lada C. J., Shu F. H., 1987, ApJ, 312, 788
Alexander R. D., Armitage P. J., 2007, MNRAS, 375, 500
Alexander R. D., Clarke C. J., Pringle J. E., 2006, MNRAS, 369, 229
Allard F., Homeier D., Freytag B., 2012, in Richards M. T., Hubeny I., eds, IAU Symposium Vol. 282 of IAU Symposium, Stellar to Substellar Model Atmospheres. pp 235–242

Table C1. New Andicam photometry for variable sources in comparison with 2MASS and DENIS

	2MASS Coordinates	Name					2MASS		DENIS	
			R	I	J	K	J	K	J	K
1	J11075730-7717262	CHXR30b	19.9	17.6	13.10	9.59	13.87	9.95	12.9,13.0,13.1	9.5,9.8,9.6
2	J11075792-7738449	FK Cha, HM16	14.38	13.30	10.40	7.25	9.50	6.83	10.4,10.8,10.2	7.2,7.5,7.3
3	J11083905-7716042	T35, ISO151	15.4	14.3	11.69	9.32	11.17	9.11	11.0,10.7	9.0,8.9
4	J11092266-7634320	C1-6, P30	-	-	-	8.6	12.60	8.67	13.3,12.5,12.6	9.4,8.9,8.7
5	J11092379-7623207	VZ Cha, T40	12.7	11.8	9.98	8.18	10.44	8.24	10.0,9.8,10.1	7.8,8.0,8.4
6	J11095340-7634255	FM Cha, HM23	14.14	12.73	9.91	7.08	8.47	6.46	10.8,10.0	6.3,7.5
7	J11113965-7620152	XX Cha, T49, Sz39	13.70	12.65	10.65	9.02	10.47	8.87	10.7,10.7	9.5,9.3

André P., Men'shchikov A., Bontemps S., Könyves V., Motte F., Schneider N., Didelon 2010, A&A, 518, L102

André P., Ward-Thompson D., Barsony M., 1993, ApJ, 406, 122

Andrews S. M., Rosenfeld K. A., Kraus A. L., Wilner D. J., 2013, ArXiv e-prints

Andrews S. M., Williams J. P., 2005, ApJ, 631, 1134

Andrews S. M., Williams J. P., 2007, ApJ, 671, 1800

Andrews S. M., Wilner D. J., Espaillat C., Hughes A. M., Dullemond C. P., McClure M. K., Qi C., Brown J. M., 2011, ApJ, 732, 42

Andrews S. M., Wilner D. J., Hughes A. M., Qi C., Dullemond C. P., 2010, ApJ, 723, 1241

Antoniucci S., García López R., Nisini B., Giannini T., Lorenzetti D., Eislöffel J., Bacciotti F., Cabrit S., Caratti o Garatti A., Dougados C., Ray T., 2011, A&A, 534, A32

Beckwith S. V. W., Sargent A. I., Chini R. S., Guesten R., 1990, AJ, 99, 924

Belloche A., Schuller F., Parise B., André P., Hatchell J., Jørgensen J. K., Bontemps S., Weiß A., Menten K. M., Muders D., 2011, A&A, 527, A145

Brown J. M., Blake G. A., Dullemond C. P., Merín B., Augereau J. C., Boogert A. C. A., Evans II N. J., Geers V. C., Lahuis F., Kessler-Silacci J. E., Pontoppidan K. M., van Dishoeck E. F., 2007, ApJ, 664, L107

Cardelli J. A., Clayton G. C., Mathis J. S., 1989, ApJ, 345, 245

Chiang E., Murray-Clay R., 2007, Nature Physics, 3, 604

Chiang E. I., Goldreich P., 1997, ApJ, 490, 368

Chiang E. I., Goldreich P., 1999, ApJ, 519, 279

Cieza L. A., Lacour S., Schreiber M. R., Casassus S., Jordán A., Mathews G. S., Cánovas H., Ménard F., Kraus A. L., Pérez S., Tuthill P., Ireland M. J., 2013, ApJ, 762, L12

Cohen M., Wheaton W. A., Megeath S. T., 2003, AJ, 126, 1090

Costigan G., Scholz A., Stelzer B., Ray T., Vink J. S., Mohanty S., 2012, MNRAS, 427, 1344

D'Alessio P., Calvet N., Hartmann L., Franco-Hernández R., Servín H., 2006, ApJ, 638, 314

D'Alessio P., Canto J., Calvet N., Lizano S., 1998, ApJ, 500, 411

D'Alessio P., Hartmann L., Calvet N., Franco-Hernández R., Forrest W. J., Sargent B., Furlan E., Uchida K., Green J. D., Watson D. M., Chen C. H., Kemper F., Sloan G. C., Najita J., 2005, ApJ, 621, 461

Davis S. S., 2005, ApJ, 627, L153

Dominik C., Blum J., Cuzzi J. N., Wurm G., 2007, Protostars and Planets V, pp 783–800

Dullemond C. P., Dominik C., 2004, A&A, 421, 1075

Dullemond C. P., Dominik C., 2005, A&A, 434, 971

Dullemond C. P., Dominik C., Natta A., 2001, ApJ, 560, 957

Espaillat C., Calvet N., D'Alessio P., et al 2007a, ApJ, 670, L135

Espaillat C., Calvet N., D'Alessio P., et al 2007b, ApJ, 664, L111

Feigelson E. D., Lawson W. A., 2004, ApJ, 614, 267

Fouqué P., Chevallier L., Cohen M., et al 2000, A&AS, 141, 313

Gauvin L. S., Strom K. M., 1992, ApJ, 385, 217

Greaves J. S., Rice W. K. M., 2010, MNRAS, 407, 1981

Griffin M. J., Abergel A., Abreu A., et al 2010, A&A, 518, L3

Henning T., Pfau W., Zinnecker H., Prusti T., 1993, A&A, 276, 129

Hildebrand R. H., 1983, QJRAS, 24, 267

Houck J. R., Roellig T. L., Van Cleve J., et al 2004, in Mather J. C., ed., Society of Photo-Optical Instrumentation Engineers (SPIE) Conference Series Vol. 5487 of Society of Photo-Optical Instrumentation Engineers (SPIE) Conference Series, The infrared spectrograph on the Spitzer Space Telescope. pp 62–76

Ireland M. J., Kraus A. L., 2008, ApJ, 678, L59

Jarrett T. H., Cohen M., Masci F., et al 2011, ApJ, 735, 112

Kim K. H., Watson D. M., Manoj P., Furlan E., Najita J., Forrest W. J., Sargent B., Espaillat C., Calvet N., Luhman K. L., McClure M. K., Green J. D., Harrold S. T., 2009, ApJ, 700, 1017

Krauss O., Wurm G., Mousis O., Petit J.-M., Horner J., Alibert Y., 2007, A&A, 462, 977

Lada C. J., 1987, in Peimbert M., Jugaku J., eds, Star Forming Regions Vol. 115 of IAU Symposium, Star formation - From OB associations to protostars. pp 1–17

Lafrenière D., Jayawardhana R., Brandeker A., Ahmic M., van Kerkwijk M. H., 2008, ApJ, 683, 844

Lee N., Williams J. P., Cieza L. A., 2011, ApJ, 736, 135

Luhman K. L., 2004, ApJ, 602, 816

Luhman K. L., 2007, ApJS, 173, 104

Luhman K. L., Allen L. E., Allen P. R., Gutermuth R. A., Hartmann L., Mamajek E. E., Megeath S. T., Myers P. C., Fazio G. G., 2008, ApJ, 675, 1375

Manoj P., Kim K. H., Furlan E., McClure M. K., Luhman K. L., Watson D. M., Espaillat C., Calvet N., Najita J. R., D'Alessio P., Adame L., Sargent B. A., Forrest W. J., Bohac C., Green J. D., Arnold L. A., 2011, ApJS, 193, 11

Mathieu R. D., Stassun K., Basri G., Jensen E. L. N.,

Johns-Krull C. M., Valenti J. A., Hartmann L. W., 1997, AJ, 113, 1841
Matrà L., Merín B., Alves de Oliveira C., Huélamo N., Kóspál A., Cox N. L. J., Ribas Á., Puga E., Vavrek R., Royer P., Prusti T., Pilbratt G. L., André P., 2012, A&A, 548, A111
Mohanty S., Greaves J., Mortlock D., Pascucci I., Scholz A., Thompson M., Apai D., Lodato G., Looper D., 2013, ArXiv e-prints
Najita J. R., Strom S. E., Muzerolle J., 2007, MNRAS, 378, 369
Olofsson J., Szűcs L., Henning T., Linz H., Pascucci I., Joergens V., 2013, ArXiv e-prints
Owen J. E., Ercolano B., Clarke C. J., 2011, MNRAS, 412, 13
Pilbratt G. L., Riedinger J. R., Passvogel T., Crone G., Doyle D., Gageur U., Heras A. M., Jewell C., Metcalfe L., Ott S., Schmidt M., 2010, A&A, 518, L1
Poglitsch A., Waelkens C., Geis N., et al 2010, A&A, 518, L2
Quillen A. C., Blackman E. G., Frank A., Varnière P., 2004, ApJ, 612, L137
Rebull L. M., Stapelfeldt K. R., Werner M. W., Mannings V. G., Chen C., Stauffer J. R., Smith P. S., Song I., Hines D., Low F. J., 2008, ApJ, 681, 1484
Ribas Á., Merín B., Bouy H., Alves de Oliveira C., Ardila D. R., Puga E., Kóspál Á., Spezzi L., Cox N. L. J., Prusti T., Pilbratt G. L., André P., Matrà L., Vavrek R., 2013, ArXiv e-prints
Ricci L., Testi L., Natta A., Neri R., Cabrit S., Herczeg G. J., 2010, A&A, 512, A15
Rice W. K. M., Wood K., Armitage P. J., Whitney B. A., Bjorkman J. E., 2003, MNRAS, 342, 79
Robberto M., Spina L., Da Rio N., Apai D., Pascucci I., Ricci L., Goddi C., Testi L., Palla F., Bacciotti F., 2012, AJ, 144, 83
Robitaille T. P., Whitney B. A., Indebetouw R., Wood K., Denzmore P., 2006, ApJS, 167, 256
Scholz A., 2012, MNRAS, 420, 1495
Scholz A., Jayawardhana R., Wood K., 2006, ApJ, 645, 1498
Scholz A., Xu X., Jayawardhana R., Wood K., Eislöffel J., Quinn C., 2009, MNRAS, 398, 873
Shirley Y. L., Evans II N. J., Rawlings J. M. C., Gregersen E. M., 2000, ApJS, 131, 249
Sicilia-Aguilar A., Kim J. S., Sobolev A., Getman K., Henning T., Fang M., 2013, ArXiv e-prints
Siess L., Dufour E., Forestini M., 2000, A&A, 358, 593
Skinner C. J., 1996, Technical report, Flux Units and NICMOS
Skrutskie M. F., Cutri R. M., Stiening R., et al 2006, AJ, 131, 1163
Watson A. M., Stapelfeldt K. R., Wood K., Ménard F., 2007, Protostars and Planets V, pp 523–538
Whittet D. C. B., Prusti T., Franco G. A. P., Gerakines P. A., Kilkenny D., Larson K. A., Wesselius P. R., 1997, A&A, 327, 1194
Williams J. P., Cieza L. A., 2011, ARA&A, 49, 67
Winston E., Cox N. L. J., Prusti T., Merín B., Ribas A., Royer P., Vavrek R., Puga E., André P., Men'shchikov A., Könyves V., Kóspál Á., Alves de Oliveira C., Pilbratt G. L., Waelkens C., 2012, A&A, 545, A145
Wright E. L., Eisenhardt P. R. M., Mainzer A. K., et al 2010, AJ, 140, 1868